ELSEVIER

The computation of flow development through stationary and rotating U-ducts of strong curvature

H. Iacovides, B. E. Launder, and H-Y. Li
Department of Mechanical Engineering, University of Manchester Institute of Science and Technology, Manchester, UK

This article presents comparisons between predictions, obtained during the course of this investigation, and recently produced measurements of the flow development through a square cross-sectioned U-bend of strong curvature, $Rc/D = 0.65$, that is either stationary or in orthogonal rotation. For the stationary case, four turbulence models have been tested; a high-Re k-ε model interfaced with the low-Re 1-equation model in the near-wall regions, a high-Re algebraic second-moment (ASM) closure with the low-Re 1-equation model in the near-wall regions, and two versions of a low-Re ASM model. The two low-Re ASM models return noticeably better predictions of the flow development. There is, however further scope for improvement, especially in the downstream section. Two rotating flow cases have been computed both with the axis of rotation parallel to the axis of bend curvature; one at a positive rotation number $R_o \equiv \Omega D/W_b$ of 0.2 and one at $R_o \equiv -0.2$. In the case of positive rotation, where the Coriolis and curvature forces reinforce each other, the flow predictions of the low-Re ASM are in very close agreement with the data. When the U-bend rotates negatively, the complex flow field generated in the downstream section is not well reproduced by the low-Re ASM model. More refined turbulence models are thus necessary when the curvature and Coriolis forces oppose each other.

Keywords: duct flow computations; strong curvature; orthogonal rotation

Introduction

The cooling arrangements in modern gas turbine blades commonly entail the circulation of "cool" air (having bypassed the combustion section) through roughly square serpentine cooling passages in the blade interior. The very tight U-bends that terminate each straight section of the passage necessarily provoke flow separation, while the flow is further complicated by the blade rotation inducing significant Coriolis and quasibuoyant forces on the flow.

The present contribution is a computational study aimed at assessing how far engineering turbulence models have progressed in enabling CFD schemes to predict flows of such complexity. Of course, in order to carry out such a comparison, we need a detailed set of experimental data; the recent availability of such a database, Cheah et al. (1994) has stimulated the present study.

There already is a substantial body of literature on the turbulent flow in curved or rotating pipes. It has been amply demonstrated that the early wall-function approach adopted by Majumdar and Spalding (1977) needs to be replaced by a low-Reynolds-number turbulence model extending across the viscosity-affected sublayer (Iacovides and Launder 1985; Taylor et al. 1985), to predict the near-wall secondary flow with sufficient accuracy. For the case of fully developed flow in straight rotating ducts, provided we resolve the viscous sublayer, a wide range of turbulence-modeling strategies adequately reproduces the Ito-Nanbu (1971) correlation of rotation effects on overall skin friction. Modeling of flow through curved ducts has brought out more decisively the advantages of adopting an algebraic second-moment (ASM) closure rather than an eddy-viscosity model (EVM) either across simply the fully turbulent region (Iacovides and Launder 1985) or, more effectively, across the viscous region also (Iacovides and Launder 1992).

Now, the flow to be examined in the present study entails a much tighter bend, which provokes a large downstream separation. Such flows have previously been examined (for zero rotation) by Besserman and Tanrikut (1991), Xia and Taylor (1993), and Bo et al. (1995). The two former studies confirmed the inadequacy of "wall functions" to provide qualitatively useful predictions; while the latter showed that, contrary to previous belief and practice, it was essential [with the types of grid density available for these fully three-dimensional (3-D) flows] to employ high-order discretization schemes for convection on the turbulent variables (k and ε) as well as the mean flow variables. (Conventional wisdom holds that a simple upwind differencing is

Address reprint requests to Dr. H. Iacovides, Department of Mechanical Engineering, UMIST, P. O. Box 88, Manchester M60 1QD, UK.

Received 28 September 1994; accepted 26 April 1995

Int. J. Heat and Fluid Flow 17: 22–33, 1996

655 Avenue of the Americas, New York, NY 10010

0142-727X/96/$15.00
SSDI 0142-727X(95)00056-V

suitable for k and ε as convection is outweighed by the important source and sink terms present in their transport equations.)

The present study provides a continuation of the work reported by Bo et al. (1995). We re-examine the stationary duct (as well as considering two rotating flow cases), because the recent data of Cheah et al. (1994) provide a far more complete flow mapping than had hitherto been available. This allows greater certainty to be reached in the assessment of the turbulence models.

Mathematical and physical model

Mean field equations

The Reynolds and continuity equations describing the motion of turbulent flow in an arbitrary rotating coordinate system may be written as follows:

$$\frac{\partial}{\partial x_j}(\rho U_i U_j) = \frac{\partial P}{\partial x_i} + \frac{\partial}{\partial x_j}\left[\mu\left(\frac{\partial U_i}{\partial x_j} + \frac{\partial U_j}{\partial x_i}\right) - \rho\overline{u_i u_j}\right] - 2\rho\varepsilon_{ipj}\Omega_p U_j - \rho(\Omega_j X_j \Omega_i - \Omega_j X_i \Omega_j) \quad (1)$$

$$\frac{\partial}{\partial x_i}(\rho U_i) = 0 \quad (2)$$

Here, U_i is the mean velocity vector: Ω_j the coordinate rotation vector, and $\overline{u_i u_j}$ the unknown Reynolds-stress tensor.

Turbulence models

The turbulent stresses are approximated by four different models, all of which involve the resolution of the wall sublayer region. All the models tested are those that have previously been employed in other duct flow computations at UMIST with at least moderate success. It was, therefore, important to establish how well these models predicted the flow development through this more realistic representation of a blade-cooling passage. The models employed are:

(1) a zonal EVM involving the high-Re k-ε model in the duct core and the low-Re one-equation model in the near-wall regions (k-ε/1-eq);
(2) a zonal model involving a second-moment high-Re ASM in the duct core and the low-Re one-equation model in the near-wall regions (ASM/1-eq);
(3) a low-Re ASM model in which, within the wall sublayers, the dissipation rate of turbulence is obtained algebraically from a prescribed length scale (ASM1); and
(4) a low-Re ASM model in which the ε transport equation is solved over the entire flow domain (ASM2).

Details of these four schemes are given below.

High-Re k-ε model. The turbulent stresses are obtained from the EVM constitutive equation:

$$\overline{u_i u_j} = \frac{2}{3}k\delta_{ij} - \nu_t\left(\frac{\partial U_i}{\partial x_j} + \frac{\partial U_j}{\partial x_i}\right) \quad (3)$$

where

$$\nu_t = c_\mu k^2/\varepsilon \quad (4)$$

The turbulent kinetic energy k is obtained from:

$$\frac{\partial}{\partial x_j}(\rho U_j k) = \frac{\partial}{\partial x_j}\left[\left(\mu + \frac{\mu_t}{\sigma_k}\right)\frac{\partial k}{\partial x_j}\right] + \rho P_k - \rho\varepsilon \quad (5)$$

where

$$P_k \equiv -\overline{u_i u_j}\frac{\partial \mathrm{U}_i}{\partial x_j} \quad (6)$$

The dissipation rate ε is obtained from:

$$\frac{\partial}{\partial x_j}(\rho U_j \varepsilon) = \frac{\partial}{\partial x_j}\left[\left(\mu + \frac{\mu_t}{\sigma_\varepsilon}\right)\frac{\partial \varepsilon}{\partial x_j}\right] + c_{\varepsilon 1}\rho\frac{\varepsilon}{k}P_k - c_{\varepsilon 2}\rho\frac{\varepsilon^2}{k} \quad (7)$$

Notation

c_1, c_2, c'_1, c'_2	
$c_{\varepsilon 1}$, $c_{\varepsilon 2}$, c_k, c_ε	turbulence modeling constants
D	hydraulic diameter
f_2, f_{H1}, f_{H2}	
f_w, f_ε, f_μ	low-Re damping functions
H_{ij}	low-Re inhomogeneity tensor
k	turbulent kinetic energy
ℓ	turbulent length scale ($\ell = k^{3/2}/\varepsilon$)
ℓ_ε	dissipation length scale
ℓ_μ	turbulent viscosity length scale
P	pressure
P_{ij}	generation rate of $\overline{u_i u_j}$
P_k	generation rate of k
R_c	radius of curvature of U-bend
R_e	flow Reynolds number ($\equiv W_b D/\nu$)
R_o	rotation number ($\equiv \Omega D/W_b$)
R_t	local Reynolds number of turbulence
U	mean velocity in crossduct direction
u	velocity fluctuation in crossduct direction
$\overline{u_i u_j}$	Reynolds stress tensor
V	mean velocity normal to the duct symmetry plane
v	velocity fluctuation normal to the duct symmetry plane
W	mean velocity in streamwise direction
w	velocity fluctuation in streamwise direction
W_b	bulk velocity
X_i	distance from the axis of rotation
x	crossduct direction
y	direction normal to the duct symmetry plane
Y	near-wall distance
y^*	dimensionless near-wall distance
z	streamwise direction

Greek

δ_{ij}	Kronecker delta
ε	dissipation rate
ε_{ipq}	third-order alternating tensor
μ	molecular viscosity
μ_t	turbulent viscosity
ν	molecular kinematic viscosity
ν_t	turbulent kinematic viscosity
ϕ_{ij1}, ϕ_{ij2}	redistribution terms
ϕ^w_{ij}	wall reflection term
Ω	angular velocity of frame of reference

High-Re ASM model. In this closure, the turbulent stresses are obtained from a truncated form of the stress transport equations as follows:

$$\frac{\overline{u_i u_j}}{k}(P_k - \varepsilon) = P_{ij} - \frac{2}{3}\varepsilon\delta_{ij} + \phi_{ij} + \phi^w_{ij} \tag{8}$$

where

$$P_{ij} \equiv -\overline{u_j u_k}\frac{\partial U_i}{\partial x_k} - \overline{u_j u_k}\frac{\partial U_i}{\partial x_k} - 2\Omega_p\left(\varepsilon_{ipq}\overline{u_q u_j} + \varepsilon_{jpq}\overline{u_q u_i}\right) \tag{9}$$

is the production rate for $\overline{u_i u_j}$.

The term ϕ_{ij} represents the redistribution of energy between the different components of the stress tensor. If buoyant and wall-reflection effects can be neglected, it consists of two parts, ϕ_{ij1} and ϕ_{ij2} given by the following:

$$\phi_{ij1} = -c_1\frac{\varepsilon}{k}\left(\overline{u_i u_j} - \frac{2}{3}k\delta_{ij}\right) \tag{10}$$

$$\phi_{ij2} = -c_2\left(P_{ij} - \tfrac{2}{3}P_k\delta_{ij}\right) \tag{11}$$

The "wall-echo" part of the pressure strain correlation ϕ^w_{ij} is approximated by the proposal of Gibson and Launder (1978).

$$\phi^w_{ij} = c'_1\frac{\varepsilon}{k}\left(\overline{u_q u_m}n_q n_m\delta_{ij} - \frac{3}{2}\overline{u_i u_q}n_q n_j - \frac{3}{2}\overline{u_j u_q}n_j n_q\right) + c'_2\left(\phi_{qm,2}n_q n_m\delta_{ij} - \frac{3}{2}\phi_{qj,2}n_q n_j - \frac{3}{2}\phi_{qi,2}n_i n_q\right)f\left(\frac{\ell}{Y}\right) \tag{12}$$

n_q is the unit vector normal to the wall in question; Y is the distance to the wall; and ℓ_ε is the local turbulent length scale defined as follows:

$$\ell_\varepsilon = k^{3/2}/\varepsilon \tag{13}$$

Although $f(\ell/Y)$ was originally devised for a single plane surface, as in all our earlier work on flows through rectangular ducts, we have simply superimposed the effects caused by the two pairs of opposite wall. For walls in the x–y and x–z planes, respectively, the wall influence functions become as follows:

$$f(\ell/n_x y) = \frac{\ell}{x} + \frac{\ell}{D-x}$$

$$f(\ell/n_y x) = \frac{\ell}{D/2-y} + \frac{\ell}{D/2+y} \tag{14}$$

The need to impose these wall-distance-based corrections is one of the weakest features of current turbulence models, and thus, it is encouraging that, in simpler flows than those considered here, progress is being made in eliminating wall reflection (Launder and Li 1994).

The k and ε transport equations are identical to those of the high-Re k-ε model, Equations 5 and 7, apart from the approximation used for the turbulent diffusion of k and ε.

$$\frac{\partial}{\partial x_j}(\rho U_j k) = \frac{\partial}{\partial x_j}\left[\left(\mu\delta_{ij} + c_k\rho\frac{k}{\varepsilon}\overline{u_i u_j}\right)\frac{\partial k}{\partial x_i}\right] + \rho P_k - \rho\varepsilon \tag{15}$$

$$\frac{\partial}{\partial x_j}(\rho U_j \varepsilon) = \frac{\partial}{\partial x_j}\left[\left(\mu\delta_{ij} + c_\varepsilon\rho\frac{k}{\varepsilon}\overline{u_i u_j}\right)\frac{\partial \varepsilon}{\partial x_i}\right] + c_{\varepsilon 1}\rho\frac{\varepsilon}{k}P_k - c_{\varepsilon 2}\rho\frac{\varepsilon^2}{k} \tag{16}$$

Low-Re one-equation model. This is the version initially proposed by Wolfshtein (1969). The turbulent stresses are approximated through the effective viscosity expression of Equation 3 and the k transport equation is identical to that of the high-Re k/ε model, Equation 5. The dissipation rate ε is obtained from the near-wall distance Y, according to:

$$\varepsilon = k^{3/2}/\ell_\varepsilon \tag{17}$$

$$\ell_\varepsilon = 2.55Y[1 - \exp(-0.263y^*)] \tag{18}$$

where $y^* \equiv 2.55Yk^{1/2}/\nu$.

The turbulent viscosity ν_t is obtained from:

$$\nu_t = c_\mu\ell_\mu k^{1/2}$$

$$\ell_\mu = 2.55Y[1 - \exp(0.016y^*)] \tag{19}$$

Low-Re ASM models. In both versions of the low-Re ASM model employed, the turbulent stresses are obtained from an equation that has the same overall form:

$$(P_k - \varepsilon)\frac{\overline{u_i u_j}}{k} = P_{ij} - \varepsilon_{ij} + \phi_{ij} + f_w\phi^w_{ij} + f_{H1}\left(H_{ij} - \frac{1}{3}H_{kk}\delta_{ij}\right) + f_{H2}k\left(\frac{\partial U_i}{\partial x_j} + \frac{\partial U_j}{\partial x_i}\right) \tag{20}$$

where

$$\varepsilon_{ij} = \frac{2}{3}(1 - f_\varepsilon)\varepsilon\delta_{ij} + f_\varepsilon\frac{\overline{u_i u_j}}{k}\varepsilon \tag{21}$$

$$H_{ij} = \left(\overline{u_i u_\ell}\frac{\partial\sqrt{k}}{\partial x_\ell}\frac{\partial\sqrt{k}}{\partial x_j} + \overline{u_\ell u_j}\frac{\partial\sqrt{k}}{\partial x_i}\frac{\partial\sqrt{k}}{\partial x_\ell}\right) \tag{22}$$

For ASM 1

$$f_\varepsilon = \exp(-y^*/4)$$

$$f_w = (1 - \exp[-0.12y^*])(1 + \exp[-0.03y^*])$$

$$f_{H1} = (13 + y^*)\exp(-0.07y^*)$$

$$f_{H2} = 0.06\exp(-y^*/8) \tag{23}$$

The k and ε transport equations are the same as Equations 16 and 17 for the high-Re ASM model.

Within the near-wall regions, the distribution of ε is obtained from a prescribed length scale ℓ_ε, where, following Iacovides and Li (1993):

$$\ell_\varepsilon = 2.55Y[1 - \exp(-0.236y^*)] \tag{24}$$

Although Equation 24 is similar to Equation 18, the constant within the damping function has a different value in the ASM treatment.

The k transport equation is identical to Equation 16 for the high-Re ASM model.

For ASM 2

$$f_\varepsilon = \exp(-R_t/12)$$

$$f_w = [1 - \exp(-R_t/20)][1 + \exp(-R_t/100)]$$

$$f_{H1} = (15.6 + 2.4R_t)\exp(-R_t/20)$$

$$f_{H2} = 0.06\exp(-R_t/8) \tag{25}$$

where $R_t \equiv k^2/\nu\varepsilon$.

The dissipation rate ε is obtained from $\tilde{\varepsilon}$ according to:

$$\varepsilon = \tilde{\varepsilon} + 2\nu\left(\frac{\partial\sqrt{k}}{\partial x_j}\right)^2 \tag{26}$$

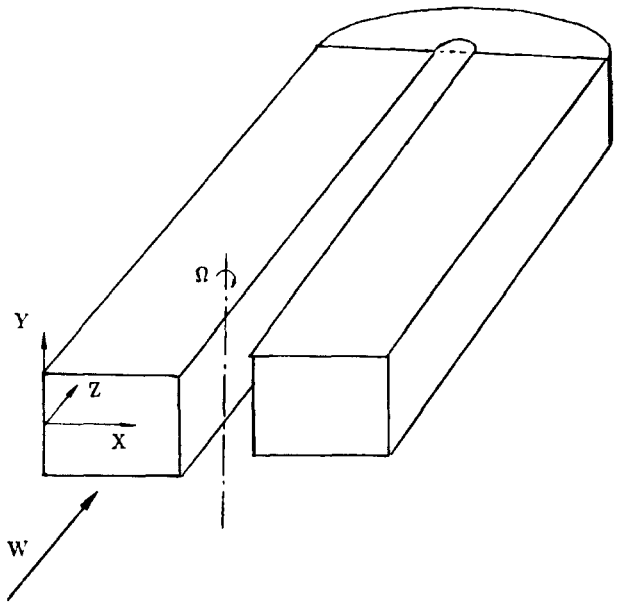

Figure 1 Flow geometry

Following Iacovides and Launder (1992), the variable ε is obtained from a transport equation similar to that proposed by Launder and Sharma (1974).

$$\frac{\partial}{\partial x_j}(\rho U_j \tilde{\varepsilon}) = \frac{\partial}{\partial x_j}\left[\left(\mu\delta_{ij} + c_\varepsilon \overline{u_i u_j}\frac{\tilde{\varepsilon}}{\tilde{k}}\right)\frac{\partial \tilde{\varepsilon}}{\partial x_i}\right] + c_{\varepsilon 1}\rho\frac{\varepsilon}{k}P_k - c_{\varepsilon 2}f_2\rho\frac{\tilde{\varepsilon}^2}{k} + E \quad (27)$$

where

$$E \equiv 2\rho\nu\nu_t\left(\frac{\partial^2 U_i}{\partial x_j \partial x_\ell}\right)^2 \quad (28)$$

$$f_2 = 1 - \exp(-R_t/36) \quad (29)$$

$$\nu_t = c_\mu f_\mu k^2/\tilde{\varepsilon} \quad (30)$$

$$f_\mu = \exp\left[\frac{-2.9}{(1+0.003R_t)(1+0.004R_t)}\right] \quad (31)$$

The constants that appear in the turbulence model equations take the values shown in Table 1.

Numerical aspects

Computations have been carried out using a three-dimensional (3-D) finite-volume solver. The scheme adopts the SIMPLE pressure correction method and employs a staggered grid arrangement. Full details can be found in Li (1995). Use of the second-moment ASM closure necessitated employment of a number of stabilization measures, such as the iterative solution of the stress equations, the staggering of the turbulence stresses, and the apparent viscosity concept. Details of these practices can be found in Iacovides and Launder (1985).

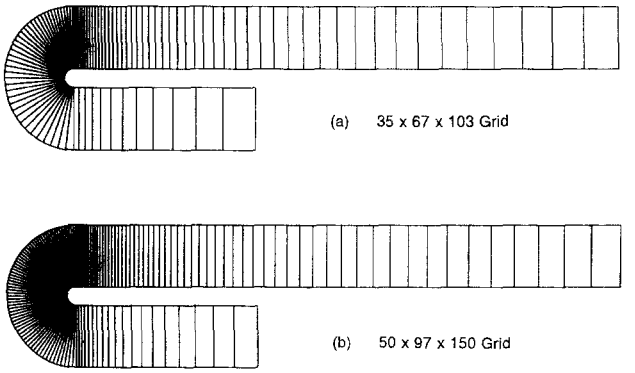

Figure 2 Grids employed; (a) 35×67×103 grid; (b) 50×97×150 grid

As recommended by Bo et al. (1985), in order to minimize numerical errors, the convective terms of all the transport equations are discretized using the LODA scheme, a bounded version of the quadratic upstream interpolation scheme developed by Zhou and Leschziner (1988). The stabilization measures necessary to implement this scheme in a turbulent 3-D code are described in Bo et al.

Computational details

The cases examined involve developing flow entering a U-bend of square cross section with a curvature ratio $Rc/D = 0.65$. The flow Reynolds number is 100,000. Three flow cases have been computed, one for flow through a stationary U-bend and two cases in which the duct rotates orthogonally with the axis of rotation parallel to the axis of curvature, as shown in Figure 1. In this mode of rotation, the curvature and Coriolis forces act in the same direction, and, consequently, the geometrical plane of symmetry remains a plane of flow symmetry. In one of the two rotating cases, the U-bend rotated positively at a rotation number ($R_o \equiv \Omega\ D/W_b$) of $+0.2$, and in the other case, negatively with the same magnitude of $R_o = -0.2$. Thus, positive rotation denotes the situation in which the trailing (pressure) side of the rotating duct coincides with the outer side of the U-duct. Thus, in positive rotation, the Coriolis and curvature forces reinforce each other; whereas, in negative rotation, these forces oppose one another.

Two grid arrangements were employed to cover the U-bend, the 3-diameter-long upstream section and the downstream section, which was 9 diameters long. For the first three models, a mesh consisting of $35 \times 67 \times 103$ nodes in the normal, radial, and streamwise directions, respectively, was employed. Of the 103 streamwise planes, 13 were distributed in the upstream tangent, 40 within the U-bend, and 50 in the downstream tangent, as shown in Figure 2(a). For ASM2, a $50 \times 97 \times 150$ mesh was used, consisting of 20 planes in the upstream section, 70 planes within the bend, and 60 planes downstream, as shown in Figure 2(b). The grid sensitivity tests of Bo et al. (1995) showed that, provided a high-order scheme was used for the discretization of convective transport, these grids were sufficiently fine to prevent

Table 1 Turbulence modeling constants

$c_{\varepsilon 1}$	$c_{\varepsilon 2}$	σ_k	σ_ε	c_μ	c_1	c_2	$c_1' r$	$c_2' r$	c_k	c_ε
1.44	1.92	1.0	1.22	0.09	1.8	0.6	0.5	0.3	0.22	0.15

numerical errors from contaminating the solutions. For the full low-Re ASM model (ASM2), using the LODA discretization scheme in all transport equations, 26 CPU seconds were needed for each iteration on the $50 \times 97 \times 150$ mesh on a CRAY-YMP supercomputer. The corresponding CPU time for the HYBRID scheme was 19 seconds. To obtain a fully converged solution, using this combination of grid and turbulence model and with the HYBRID discretization scheme, around 5000 iterations were carried out. A further 7000 iterations were necessary for the LODA solution. In the other computations, which involved less complicated turbulence models and fewer grid nodes, the number of iterations required, and the CPU time per iteration were considerably lower, reducing the overall CPU time required by at least a factor of 5. For the stationary case, computations were obtained using all four models presented in the mathematical and physical model, Section 2. For the two rotating cases, only the simplified low-Re ASM model, ASM1, was used for reasons discussed in the following sections.

Entry conditions at three diameters upstream of the bend entry, which best matched the available measurements, were generated from separate computations of developing flow in straight ducts.

Presentation and discussion of results

Stationary U-bend

The vector plots of Figure 3 present comparisons between the measured velocity field and the flow field predicted by the simplified low-Re ASM model, ASM1, along the symmetry plane of the duct and along a plane 0.125 diameters from the top wall. The measurements suggest that the flow development is dominated by the strong streamwise pressure gradients that prevail at the entry to and the exit from the U-bend. At the bend entry, there is a strong flow acceleration along the inner wall. By the 90° plane, the flow has detached from the inner wall, and the separated flow region grows as the fluid moves downstream, causing flow acceleration along the outer wall. Along the symmetry plane, reattachment occurs at 1.7 diameters downstream of the U-bend, followed by rapid recovery, while, near the top wall, the separation bubble appears to be longer and, after reattachment, recovery proceeds more slowly. The low-Re ASM model is able to reproduce the flow evolution within the U-bend, but fails to predict some of the features in the downstream flow. For the symmetry plane, a longer separation bubble is computed, and the predicted recovery after reattachment is slower. Along the near-wall plane, the ASM model returns a shorter separation bubble and different velocity distributions at one and three diameters downstream of the bend exit.

More detailed comparisons between measured profiles of the streamwise velocity and those computed with the four turbulence models are presented in Figure 4. Because of the relatively small differences in the predictions returned by the two low-Re ASM models (ASM1 and ASM2), ASM2 computations are presented at only a limited number of traverse locations in this and in most subsequent profile plots. The symmetry plane comparisons indicate that with the $k-\varepsilon$/1-eq model, the prediction of separation along the inner wall is delayed by at least 45°, the separation bubble is considerably narrower than the measured one, and the reverse flow is weaker. As the ASM/1-eq computations reveal, introduction of a second-moment closure in the duct core results in some improvements in the prediction of separation along the inner wall, especially downstream of the bend exit. The ASM1 computations demonstrate, however, that substantial improvements in the predicted flow development within the U-bend can only be achieved when the second-moment closure is extended across the wall sublayers. The solution of the ε transport equation across the sublayer region produces further, but relatively small, improvements in the computed mean flow development along the symmetry plane of the U-bend. These findings are, on the whole, consistent with those of our earlier numerical studies of unseparated duct flows (Choi et al. 1989; Iacovides et al. 1990; Iacovides and Launder 1992). Even the most refined of these models does, however, predict a somewhat delayed inner wall separation along the symmetry plane, which probably accounts for the delayed prediction of reattachment in the downstream region. Along the near-wall plane, Figure 4b, the predictions from the different models are closer to each other and are also in better accord with the data.

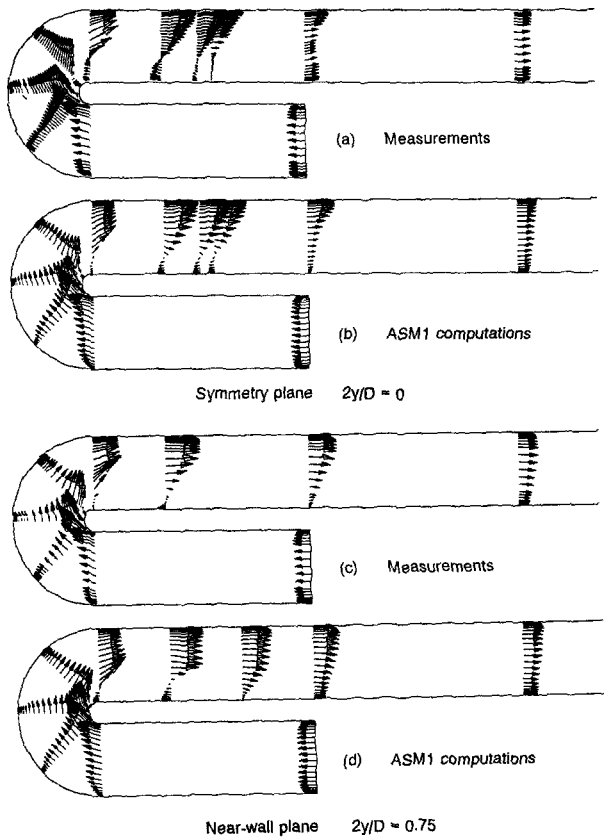

Figure 3 Comparisons of the mean flow development for stationary U-bend: (a) measurements at symmetry plane, $2y/D = 0$; (b) ASM1 computations at symmetry plane, $2y/D = 0$; (c) measurements at near-wall plane, $2y/D = 0.75$; and (d) ASM1 computations at near-wall plane, $2y/D = 0.75$

The plots of Figure 5 present similar comparisons for the cross-duct velocity component. The positive velocities at $z/D = 0$ indicate that the strong inward motion at the bend entry, associated primarily with the (inviscid) coupling of the mean velocity and pressure fields, is (naturally) well reproduced by all models. Along the symmetry plane however, all models predict that the subsequent reversal in the direction of the cross-duct motion proceeds at a rate slower than that indicated by the data. Consistent with the streamwise velocity comparisons, as the turbulence model is successively refined, the predicted cross-duct velocity profiles along the symmetry plane move closer to the measured ones. The most substantial improvements arise from the extension of the second-moment closure across the wall sublayers. Again, the integration of the ε transport equations across the near-wall regions results in further (but small) improvements in the low-Re ASM predictions. Even the most advanced of the models employed, however, returns an unrealistically slow rate of

development for the cross-duct motion. As can be seen in Figure 5b, closer to the top wall, the predictions of the different models are closer to each other and are also in better agreement with the data.

Comparisons between the measured and computed turbulent stresses provide further evidence of the models' ability to reproduce the flow development. Profile comparisons for the streamwise component of the normal stress are presented in Figure 6. The symmetry plane comparisons, Figure 6a, indicate that the $k-\varepsilon$/1-eq EVM returns a uniform distribution for the streamwise component of the normal stress. As the ASM/1-eq model computations reveal, the introduction of a second-moment closure in the duct core results in substantial improvements in the predicted distribution of the normal stress within and downstream of the bend. This comparison confirms earlier findings regarding the unsuitability of the effective viscosity approximations in flows with streamline curvature. The additional, and equally substantial, improvements in the predicted stress profiles, produced by the extension of the second-moment closure across the wall sublayers, suggest that the modeling of the near-wall regions is very important and also that the anisotropy of the near-wall turbulence is very influential in the overall flow development. The low-Re ASM model returns a stress distribution fairly similar to the experimental one, but notable discrepancies are still present. The comparisons along the near-wall plane, shown in Figure 6b, once again indicate that there are fewer differences among the predictions of the different models, which are generally in closer accord with the measurements.

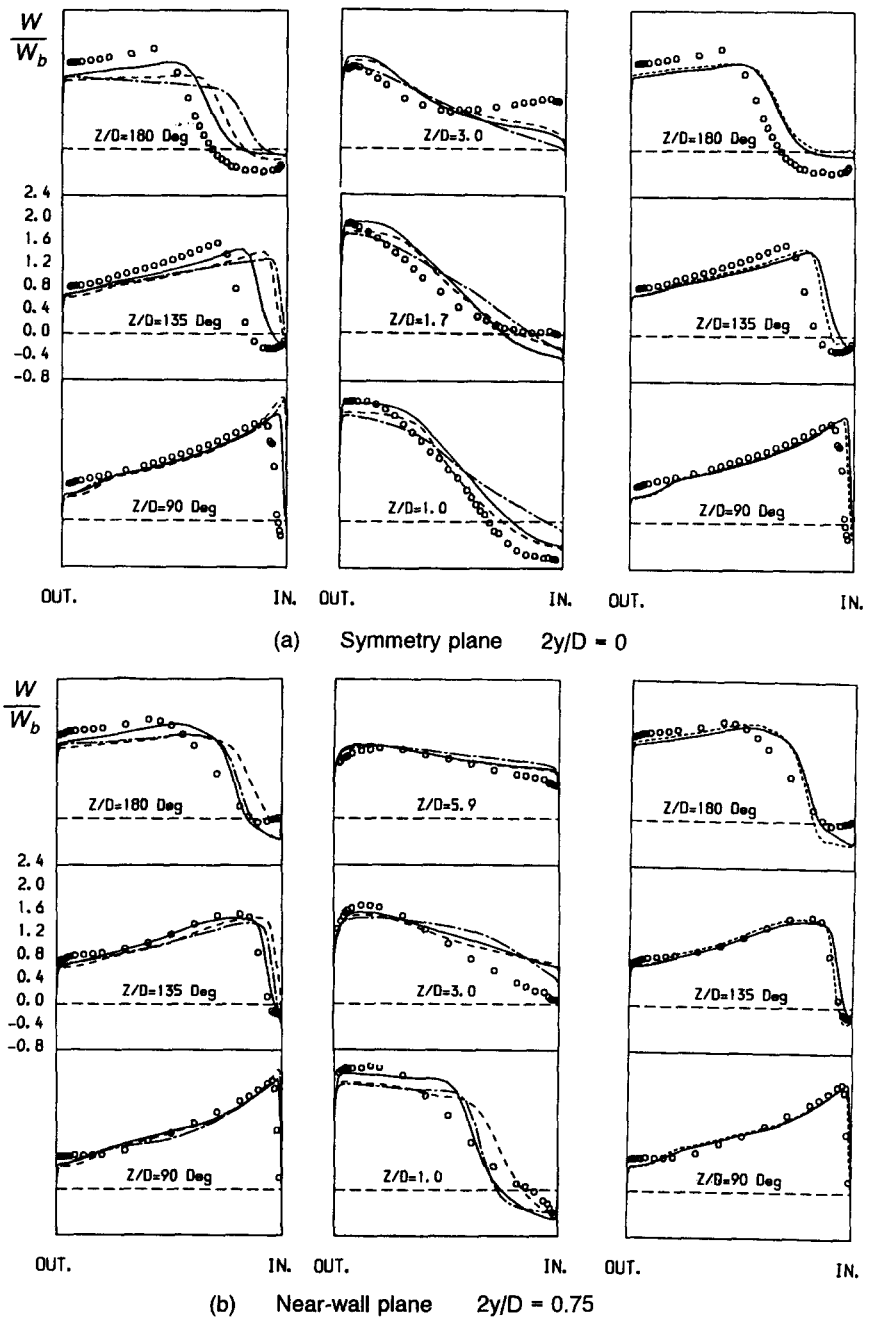

Figure 4 Comparisons of streamwise velocity profiles for stationary U-bend; o o o: data, — - —: k-ε/1-eq — —: ASM/1-eq, —: ASM1, - - -: ASM2; (a) symmetry plane $2y/D = 0$; (b) near-wall plane $2y/D = 0.75$

Figure 7 shows the corresponding comparisons for the turbulent shear stress along the streamwise and cross-stream directions. Along the symmetry plane, the EVM returns unrealistically high shear stress levels within the U-bend; while, downstream of the exit, it fails to capture the high shear stresses measured over this region. As the turbulence model is successively refined, the computed shear stress profiles move progressively closer to the measured ones. Even with the low-Re ASM closure, however, some discrepancies are still present, especially at the exit plane where the sign of the predicted shear stress is opposite that of the measured profile. Along the near-wall plane, Figure 7b, the differences in the predictions of the three models begin to diminish, and the effective viscosity model no longer over-predicts the shear stress levels within the U-bend. The low-Re ASM predictions are, again, significantly closer to the measurements, but notable discrepancies are still present.

Comparisons of Figures 3 to 7 reveal that, in computing flow through a stationary U-duct of strong curvature, it becomes necessary to employ a nonisotropic model of turbulence within the near-wall regions as well as in the duct core. Use of the low-Re ASM models produced mean and turbulent flow fields closer to the measurements than computations with models involving the effective viscosity approximation. However, because the two low-Re ASM models returned similar flow predictions for the stationary case, only the simpler ASM1 version was used in the subsequent computations of the rotating flow cases.

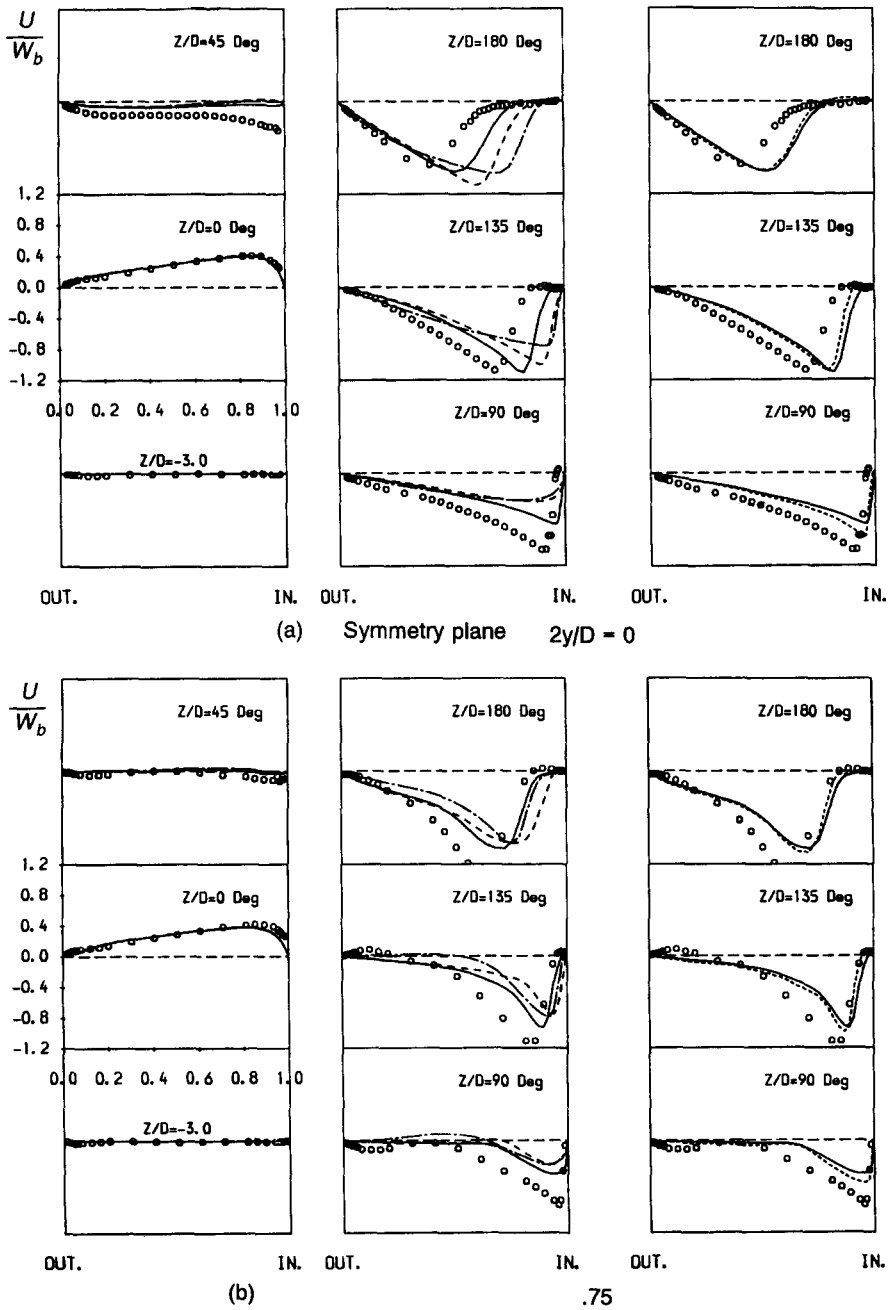

Figure 5 Comparisons of cross-duct velocity profiles for stationary U-bend; o o o: data, — - —: k-ε/1-eq — —: ASM/1-eq, —: ASM1, - - -: ASM2; (a) symmetry plane $2y/D = 0$; (b) near-wall plane $2y/D = 0.75$

U-bend in positive rotation

The vector plots of Figure 8 provide comparisons between the measured development of the mean flow field and that predicted by the low-Re ASM model, ASM1, for a positively rotating U-bend at $R_o = 0.2$. In the presence of positive rotation, for which the Coriolis force reinforces the curvature force, the low-Re ASM predictions are in better agreement with the measurements, both within the U-bend and also in the downstream region, than for the nonrotating case. The size of the now extended separation bubble is well predicted, both on the symmetry plane and the near-wall plane. The shapes of the velocity profiles, and the slower rate of recovery over the downstream tangent, are also well reproduced. Along the symmetry plane, the computed reverse flow is weaker than that measured, whereas, along the near-wall plane, the computed reverse flow is somewhat stronger. On the whole, the computed flow development for a positively rotating U-bend is encouragingly close to that determined experimentally.

Comparisons between computed and measured profiles of the streamwise component of the normal stress are shown in Figure 9. The trends present in the measurements are well reproduced both within the bend and in the downstream region. As also seen in the corresponding comparisons for the stationary U-bend, Figure 6, agreement between computations and measurements is especially good along the near-wall plane. The high turbulence levels measured in the downstream section are well reproduced by the low-Re ASM model.

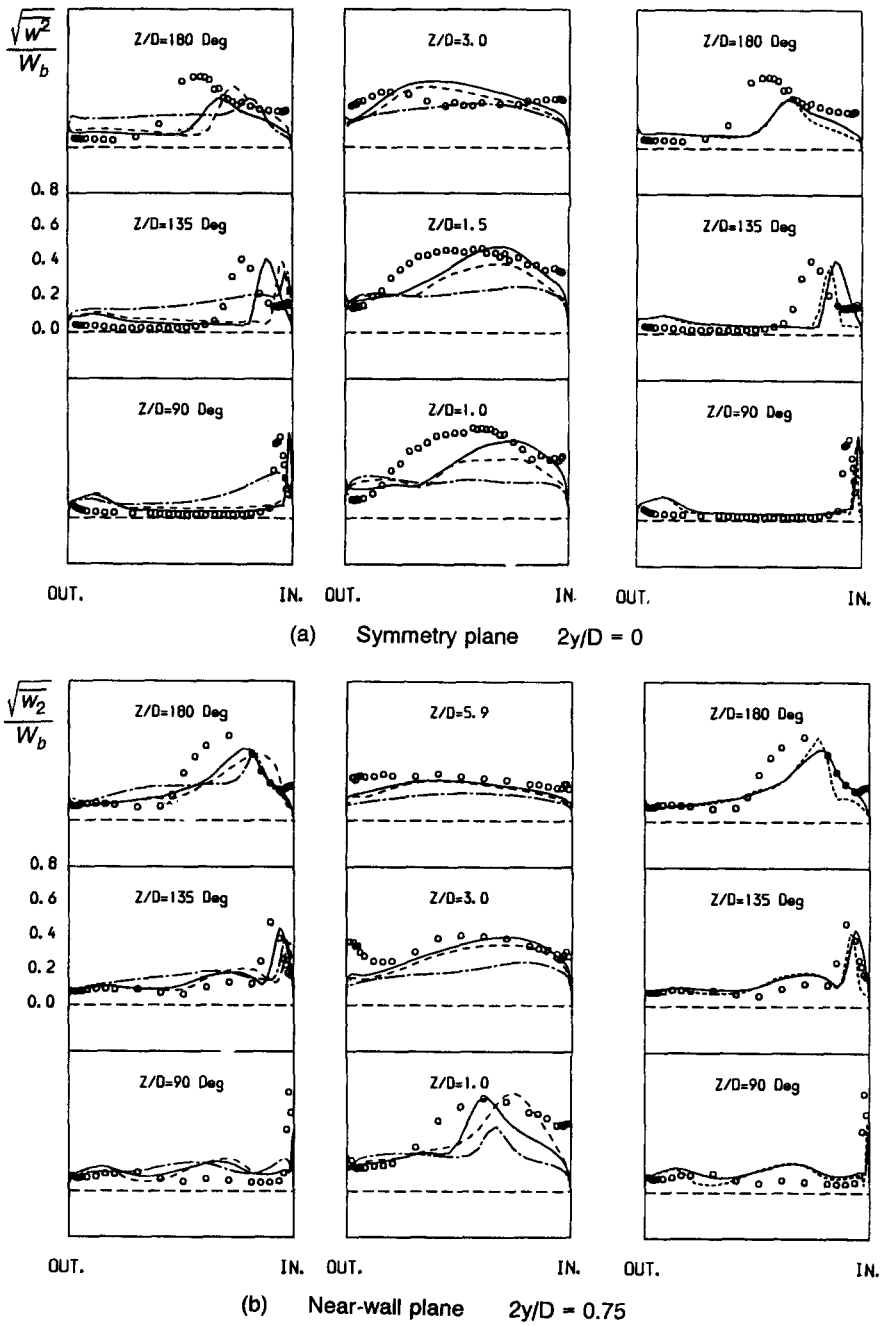

Figure 6 Comparisons of profiles of the streamwise component of the normal turbulent stress for stationary U-bend; o o o: data, — - —: k-ε/1-eq, — —: ASM/1-eq, —: ASM1, - - -: ASM2; (a) symmetry plane $2y/D = 0$; (b) near-wall plane $2y/D = 0.75$

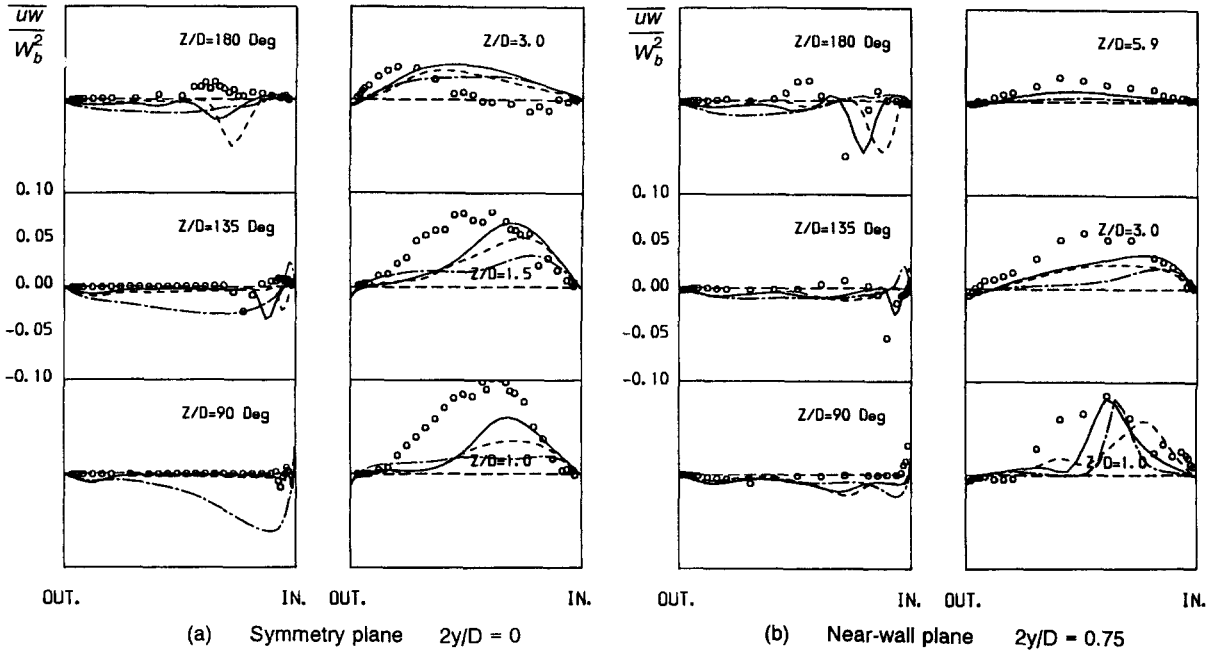

Figure 7 Comparisons of turbulent shear stress profiles for stationary U-bend; o o o: data, — - —: k-ε/1-eq; — —: ASM/1-eq, —: ASM1, – – –: ASM2; (a) symmetry plane $2y/D = 0$; (b) near-wall plane $2y/D = 0.75$

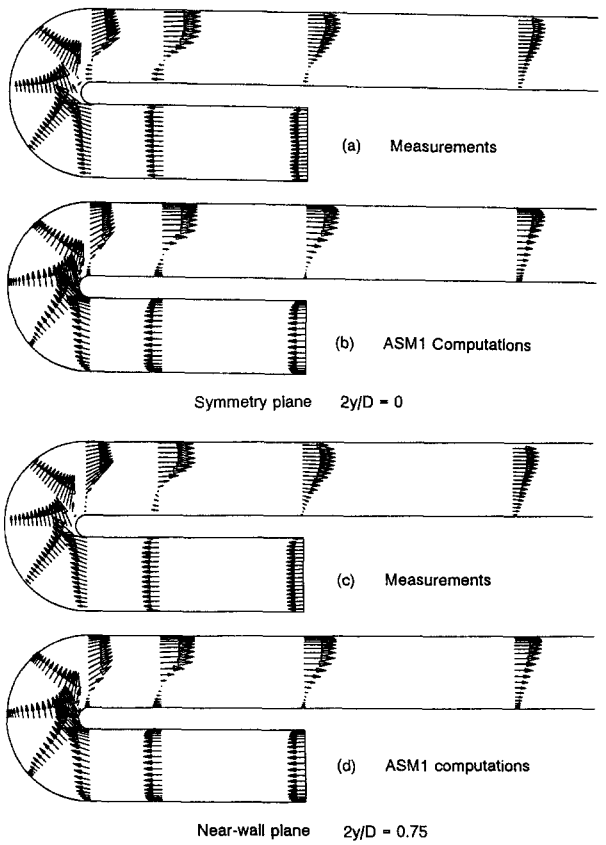

Figure 8 Comparisons of the mean flow development for a U-bend in positive rotation at $R_o = 0.2$: (a) measurements at symmetry plane, $2y/D = 0$; (b) ASM1 computations at symmetry plane, $2y/D = 0$; (c) measurements at near-wall plane, $2y/D = 0.75$; and, (d) ASM1 computations at near-wall plane at $2y/D = 0.75$

Negative rotation

Comparisons between the computed and the measured flow development at a rotation number of -0.2 are presented in Figure 10. When the Coriolis force opposes the curvature force, a more complex flow field is produced, with an additional separation region along the outer wall at the bend entry and a rapid recovery in the downstream region associated with the reversal of the secondary flow as the Coriolis force again dominates. This reversal produces the transfer of high momentum fluid from the outer to the inner wall. The low-Re ASM reproduces the measured flow separation at the bend entry and also the flow development within the bend but fails to capture all the complex flow features of the downstream section. In contrast to the cases of zero and positive rotation, discrepancies between the computed and measured downstream flow developments are now greater along the near-wall plane.

Comparisons of the streamwise component of the normal stress, shown in Figure 11, indicate that all the trends present in the measurements are reproduced by the computations, including the high-turbulence levels within the core of the bend section and the high-turbulence levels measured at one diameter downstream of the bend exit. Although some discrepancies between the computed and measured stress distributions do exist, these do not appear to be sufficiently great to explain the failure of this model to predict the correct downstream flow behavior. For this reason, comparisons of the downstream distribution of the turbulent shear stress are also shown in Figure 12. As was seen in the stationary case Figure 7 at the bend exit plane, the sign of the computed shear stress is opposite that observed in the experiment. Along the symmetry plane, the very high shear stress levels measured at one and three diameters downstream of the bend exit are well reproduced. Along the near-wall plane, in contrast to the cases of zero and positive rotation, the low-Re ASM model fails to return a realistic shear stress distribution over the first three downstream diameters. This weakness is probably responsible for the failure of this model to reproduce the observed mean flow development. The data of Cheah et al. (1994) suggest that, for negative rotation

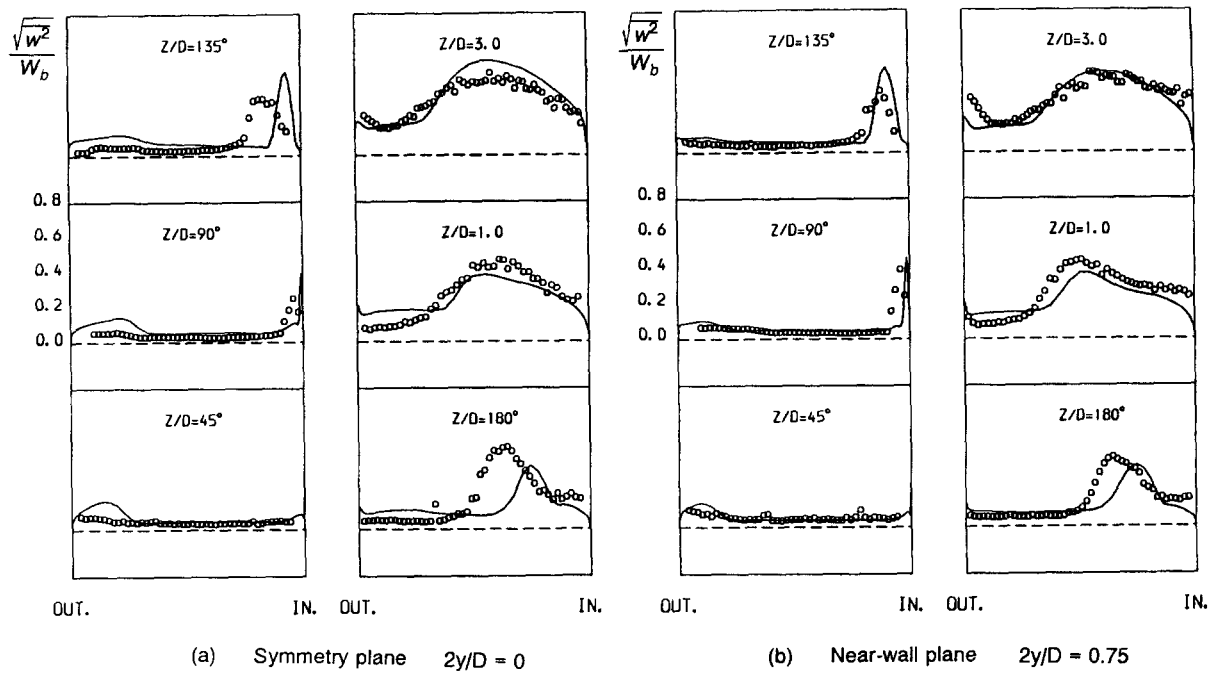

Figure 9 Comparisons of profiles of the streamwise component of the normal turbulent stress for U-bend in positive rotation at $R_o = 0.2$: o o o: data, —: ASM1; (a) symmetry plane $2y/D = 0$; (b) near-wall plane $2y/D = 0.75$

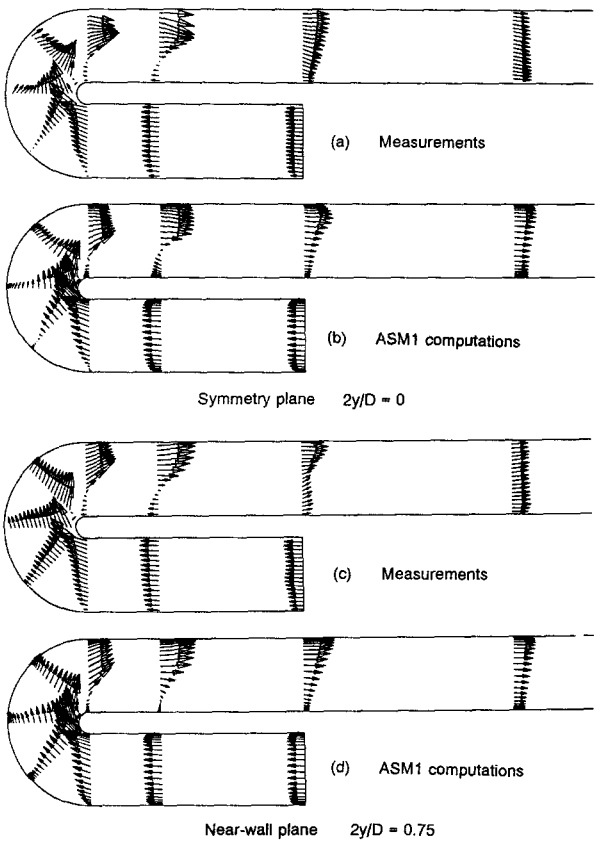

Figure 10 Comparisons of the mean flow development for a U-bend in negative rotation at $R_o = -0.2$: (a) measurements at symmetry plane, $2y/D = 0$; (b) ASM1 computations at symmetry plane, $2y/D = 0$; (c) measurements at near-wall plane, $2y/D = 0.75$; and (d) ASM1 computations at near-wall plane at $2y/D = 0.75$

in particular, diffusive transport of the turbulent stresses becomes influential over the first three downstream diameters. This is obviously a process that, within an ASM closure, is represented in an oversimplified manner.

Conclusions

In this study, the recent LDA measurements of Cheah et al. (1994) have been used to explore turbulence modeling issues related to duct flows influenced by strong curvature and rotation. The computations of flow through a stationary U-bend suggest that turbulence anisotropy within the duct core and, even more so, within the wall sublayers, has a strong influence on the development of flows affected by strong curvature. Consequently, for stationary U-bends of strong curvature, low-Re second-moment closures return mean and turbulent flow predictions superior to those arising from models that involve the effective viscosity assumption. Turbulence models that employ EVMs, either throughout the flow domain or only within the wall sublayers, are found to be unable to reproduce the effects of strong streamline curvature on the turbulence field. As a result, in effective viscosity computations, the prediction of separation along the inner wall is significantly delayed. The introduction of low-Re ASM closures improves the computed flow development within the U-bend, but the flow behavior downstream of the bend exit is still not well predicted.

When the Coriolis force reinforces the curvature force, use of low-Re ASM closures results in satisfactory predictions of the flow development within and downstream of the U-bend. When the Coriolis and the curvature forces oppose each other, the low-Re ASM model is unable to capture the complex flow development downstream of the bend exit. The data produced by Cheah et al. (1994) suggest that the inability of the low-Re ASM model to produce the correct downstream flow is partly caused by the ASM truncation of the transport terms in the stress

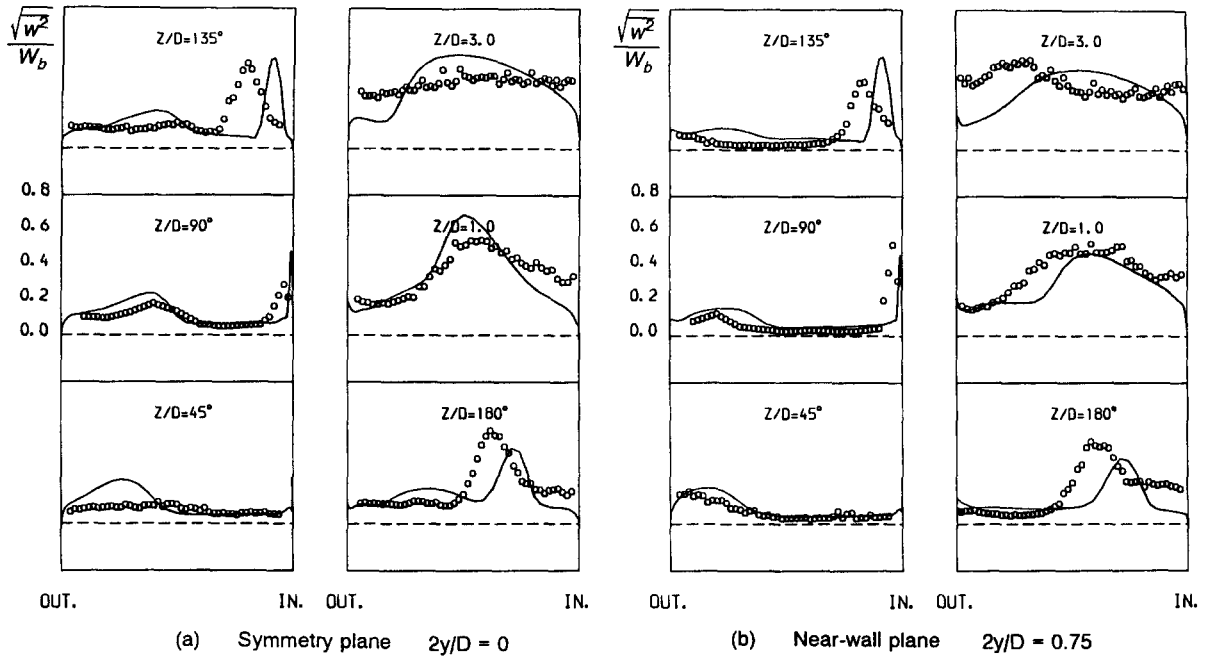

Figure 11 Comparisons of profiles of the streamwise component of the normal turbulent stress for a U-bend in negative rotation at $R_o = -0.2$: o o o: data, —: ASM1; (a) symmetry plane $2y/D = 0$ (b) near-wall plane $2y/D = 0.75$

equations. However, other refinements are simultaneously needed, perhaps the two most important being the form of the ε equation (designed to ensure that it does not generate excessive length scales in separated near-wall flows) and a model of the pressure strain model ϕ_{ij} that does not require wall proximity corrections ϕ_{ijw}. Although there is nothing wrong, in principle, in adopting wall proximity corrections, all versions currently available are based on the concept that the wall in question is an infinite flat surface. This notion is greatly in error for the inner U-bend surface, because there the radius of curvature of the bend is less than the turbulent length scale at only a short distance from the wall.

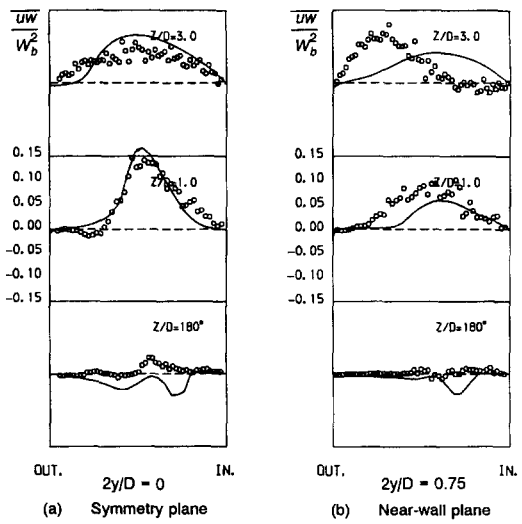

Figure 12 Comparisons of turbulent shear stress profiles for a U-bend in negative rotation at $R_o = -0.2$: o o o: data, —: ASM1; (a) symmetry plane $2y/D = 0$; (b) near-wall plane $2y/D = 0.75$

Thus, over the next few years, we must implement and refine current modeling concepts that look promising in relatively simple configurations into the computation of these sharp U-bend flows, the modeling being based on low-Re *differential* (rather than algebraic) second-moment closures.

Acknowledgments

This research was jointly supported by Rolls-Royce plc and the Defence Research Agency. We would like to thank Prof. Peter Stow and Mr. John Coupland for their interest and their technical input. Supercomputer resources were provided by the SERC. This contribution is also gratefully acknowledged. The manuscript has been produced with appreciated care by Mr. Michael Newman. Authors' names are listed alphabetically.

References

Besserman, D. L. and Tanrikut, 1991. Comparison of heat transfer measurements with computations for turbulent flow around a 180° bend. *Proc. Int. Gas Turbine Aeroengine Congress and Exposition* (ASME Paper no. 91-GT-2) Orlando, FL

Bo, T. Iacovides, H. and Launder, B. E. 1995. Convective discretization schemes for the turbulence transport equations in flow predictions through sharp U-bends, *Int. J. Num. Meth. Heat Fluid Flow*, **5**, 33–48

Cheah S. C. Iacovides H., Jackson D. C. Ji H. and Launder, B. E. 1994. LDA investigation of the flow development through rotating U-ducts. *Proc. Int. Gas-Turbine Congress and Exposition.* (ASME Paper no. 94-GT-226) The Hague

Choi Y- D., Iacovides, H. and Launder, B. E. 1989. Numerical computation of turbulent flow in a square cross-sectioned 180° bend, *J. Fluids Eng.*, **111**, 59

Gibson, M. M. and Launder, B. E. 1978. *Ground effects on pressure Fluid* fluctuations in atmospheric boundary layers. *J. Fluid Mech.*, **85**, 491

Iacovides, H. and Launder, B. E. 1985. ASM predictions of turbulent momentum and heat transfer in coils and U-bends. *Proc. 4th Int. Conference Numerical Methods Laminar and Turbulent Flow*, Swansea, Wales

Iacovides, H. Launder, B. E. Loizou, P. A. and Zhao, H. H. 1990. Turbulent boundary-layer development around a square-sectioned U-bend: Measurement and computation. *J. Fluids Eng.*, **112**, 1992

Iacovides, H. and Launder, B. E. 1992. The computation of convective heat transfer in a 180° pipe bend. *Proc. Int. Symposium on Heat Transfer in Turbomachinery*, ICHMT, Athens, Greece

Iacovides, H. and Li, H- Y. 1993. Near-wall turbulence modelling of developing flow through curved ducts and channels. *Proc. 5th Int. Symposium on Refined Flow Modelling and Turbulence Measurements*, IAHR, Paris, France

Ito, H. and Nanbu, K. 1971. Flow in rotating straight pipes of circular cross-section, *J. Basic Eng.*, **93**, 383

Launder, B. E. and Li, S. P. 1994. On the elimination of wall-topography parameters from second-moment closure, *Phys. Fluids*, **6**, 999–1006

Launder, B.E. and Sharma, B.I. 1974. Application of the energy – dissipation model of turbulence to the calculation of flow near a spinning disc. *Letters in Heat Mass Transfer*, **1**, 131–138

Li, H- Y. 1995. Ph.D. Thesis, Department of Mechanical Engineering, UMIST, Manchester, UK

Majumdar, A. K. and Spalding, D. B. 1977. A numerical investigation of three-dimensional flows in a rotating duct by a partially parabolic procedure, ASME Paper no. 77-WA/F6-7

Taylor, C. Rance, C. and Medwell, J. O. 1985. A method for the prediction of Coriolis-induced secondary flows and their influence on heat transfer in rotating ducts. *Eng. Comput*, **2**, 2–12

Wolfshtein, M. 1969. The velocity and temperature distribution in a one-dimensional flow with turbulence augmentation and pressure gradient. *Int. J. Heat Mass Transfer*, **12, 301**

Xia, J. Y. and Taylor, C. 1993. The prediction of turbulent flow and heat transfer in a tight square sectioned 180° bend, *Proc. 8th Int. Conference Numerical Methods Laminar and Turbulent Flow*, Swansea, Wales

Zhou, H. and Leschziner, M. A. 1988. A local oscillation-damping algorithm for higher-order convection schemes. *Computer Methods App. Mech. Eng.*, **67**, 355